Nanoscale

Accepted Manuscript

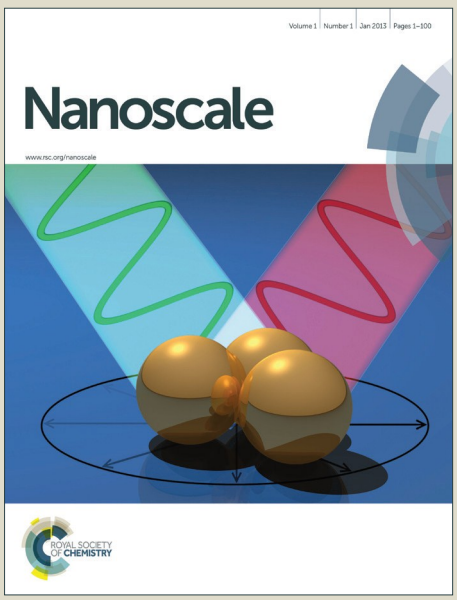

ROYAL SOCIETY OF CHEMISTRY

www.rsc.org/nanoscale

Journal Name

ARTICLE

One-Pot Pyrolysis of Lithium Sulfate and Graphene Nanoplatelet Aggregates: In situ Formed Li_2S/Graphene Composite for Lithium–Sulfur Batteries

Received 00th January 20xx,
Accepted 00th January 20xx

DOI: 10.1039/x0xx00000x

www.rsc.org/

Zhe Li, [†] Shiguo Zhang, [†] Ce Zhang, Kazuhide Ueno, Tomohiro Yasuda, Ryoichi Tatara, Kaoru Dokko, and Masayoshi Watanabe*

Lithium sulfide (Li_2S) as a cathodic material in Li–S batteries can not only deliver a high theoretical specific capacity of 1166 mAh/g, but also is essential for batteries using Li-free anode materials such as silicon and graphite. Various efforts have been made to synthesize a highly efficient Li_2S–carbon composite; however, the electronically and ionically insulating nature and high melting point of Li_2S strongly complicate the synthetic procedures, making it difficult to realize the expected capacity. Herein, a very simple method is proposed to prepare Li_2S/graphene composites by one-pot pyrolysis of a mixture of graphene nanoplatelet aggregates (GNAs) and low-cost lithium sulfate (Li_2SO4). For the first time, the entire pyrolysis process is clarified by thermogravimetry-mass spectrometry, wherein GNAs were found to partly serve as a carbon source to reduce Li_2SO_4 to Li_2S, while the remaining GNAs formed thin graphene sheets as a result of this in-situ etching, as a highly conductive host can immobilize the generated Li_2S by intimate contact. Consequently, the obtained Li_2S/graphene composite, combined with a Li_2S_x -insoluble (x = 4-8) electrolyte developed by our group, exhibits excellent electrochemical behavior for Li–S batteries.

Introduction

Conventional Li-ion batteries (LIBs), which typically consist of a graphite anode and a lithium transition-metal oxide cathode and operate according to the intercalation–deintercalation mechanism, have dominated the rechargeable battery market for more than two decades. However, they deliver energy densities of no more than 387 Wh/kg,[1] which is insufficient to meet the rapidly increasing power requirements for portable electronics and electric vehicles. Moreover, the development of large-scale grid-based energy storage systems for sustainable and renewable sources (such as wind and solar) has triggered the development of novel rechargeable electrochemical devices with higher energy density, lower cost, and longer cycle life than conventional LIBs.[2, 3] Lithium–sulfur (Li–S) batteries, a promising "beyond Li-ion" technology, have attracted considerable attention recently.[4-12] Sulfur is naturally abundant and environmentally friendly, and, importantly, can deliver a theoretical specific capacity of 1672 mAh/g and a theoretical energy density of 2600 Wh/kg or 2800 Wh/L when fully discharged, which are far greater than those of state-of-the-art LIBs.[13] Although considerable advances in Li–S batteries have been made, their commercialization is still hindered by several serious issues. Polysulfides are likely to be soluble and to diffuse from the cathode and dissolve in most electrolytes, which can act as a redox shuttle, resulting in a significant loss of active material, reaction with the lithium anode, fast capacity fading, and low Coulombic efficiencies.[14] The paired Li metal anode in Li–S batteries is reactive and prone to dendrite formation, posing some potential safety hazards. Furthermore, the active sulfur is known to undergo a large volume expansion/contraction (ca. 80%) during discharge–charge, and this induces an unstable electrochemical contact over long cycles and degrades the structural integrity of the cathode.

As an alternative active material, lithium sulfide (Li_2S) could deliver an acceptable theoretical specific capacity of 1166 mAh/g while overcoming most of the problems associated with the sulfur cathode.[4] For example, Li_2S can be paired with some high-capacity Li-free anodes such as tin and silicon,[15, 16] avoiding the formation of lithium dendrites. In addition, Li_2S (the fully lithiated state of sulfur) is at the maximum volume, so volumetric shrinkage instead of expansion occurs during the initial charge process, making the cathode mechanically stable. However, as with the sulfur cathode, Li_2S is neither electronically nor ionically conductive, making it difficult to achieve high utilization and realize the projected capacity. Various efforts have been made to ameliorate this problem by improving the contact between Li_2S and electronic conductors. Because its high melting point (938 °C) makes it impossible to incorporate Li_2S into porous conductive hosts using the

[†] These authors contributed equally to this work.
Department of Chemistry and Biotechnology, Yokohama National University, 79-5 Tokiwadai, Hodogaya-ku, Yokohama 240-8501, Japan
E-mail: mwatanab@ynu.ac.jp
† Electronic Supplementary Information (ESI) available: FESEM, AFM and cycling performance. See DOI: 10.1039/x0xx00000x

established melting–diffusion method for sulfur, most Li_2S/C composite cathodes were fabricated via direct high-energy ball-milling of commercial Li_2S powder with carbon materials, which inevitably produces a wide particle size distribution and random morphology of Li_2S and thus poor cell performance.[17-20] A solution-based route has also been pursued by dispersing carbon hosts into an ethanol–Li_2S solution,[21, 22] which is still a physical mixing process. Thermal treatment of a Li_2S_3–polyacrylonitrile composite could result in the formation of a Li_2S/C composite via chemical reactions at elevated temperatures, although this step was accompanied by the release of harmful H_2S.[23] For the methods described above, commercial bulk Li_2S powders were employed as the starting material, which may not be an attractive candidate for practical application because of its high cost. Other wet chemistry approaches were also implemented to synthesize Li_2S/C composites by means of the reaction between sulfur and organolithium reagents such as lithium triethylborohydride ($LiEt_3BH$)[15, 24, 25] or *n*-butyllithium.[16] Nevertheless, these costly, dangerous, complex procedures are difficult to handle and unsuitable for large-scale production.

In this work, we demonstrated a facile, low-cost, scalable, and environmentally friendly method for one-pot synthesis of a Li_2S/graphene composite through direct pyrolysis of a mixture of graphene nanoplatelet aggregates (GNAs) and low-cost lithium sulfate (Li_2SO_4). The GNAs have two functions: Part of them serve as a reductant to reduce Li_2SO_4 and create Li_2S at elevated temperature ($Li_2SO_4 + 2C \rightarrow 2CO_2 \uparrow + Li_2S$);[26] meanwhile, GNAs are etched in situ into thin graphene sheets via this chemical reaction. The special layered structure of these residual graphene sheets can act as a highly conductive two-dimensional (2D) host to immobilize the active Li_2S by intimate contact, facilitating the transport of electrons in the cathode[27-30] and improving the electrochemical utilization of poorly conducting Li_2S. When used as a cathode for Li–S batteries, in combination with a discharge-product-insoluble electrolyte developed by our group (where the discharge product is Li_2S_x: x = 4-8),[7, 8, 11, 31] this Li_2S/graphene composite demonstrates excellent electrochemical performance with faster reaction kinetics, lower polarization, and better cycling performance and rate capability than the physical mixture of commercial Li_2S and GNAs.

Results and Discussion

This strategy was realized by one-pot pyrolysis of Li_2SO_4 and GNAs, as depicted in **Figure 1**. First, a composite of Li_2SO_4/GNAs was obtained through a solvent/nonsolvent precipitation method (see the experimental section for details). More specifically, $Li_2SO_4 \cdot H_2O$ and GNAs (specific surface area: 750 m^2/g) were first dispersed into ultrapure water to form a suspension. Then ethanol as a precipitant of Li_2SO_4 was added dropwise into the suspension, which allows slow deposition of Li_2SO_4 onto the surface of the GNAs. After filtering, washing, and drying, the resultant black powder (**LS-GNAs C**) was subjected to pyrolysis at an elevated temperature. To set an appropriate pyrolysis temperature and elucidate the pyrolysis process of LS-GNAs C, thermogravimetry-mass spectrometry (TG-MS) measurement was conducted. As shown in **Figure 2**, two clear

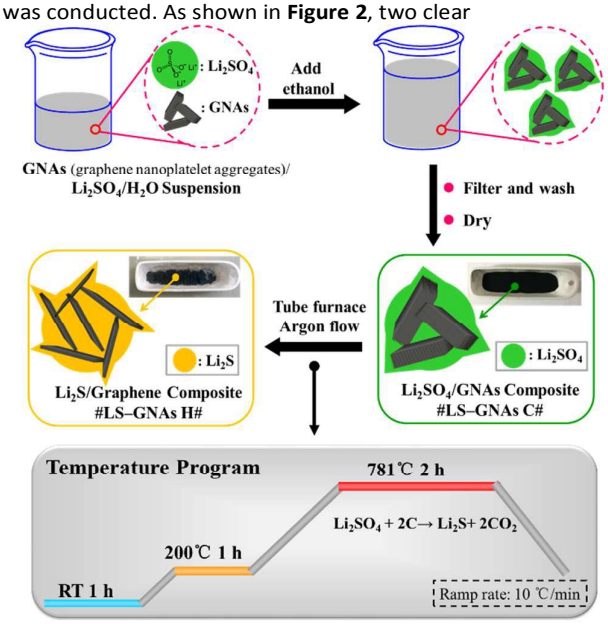

Figure 1. Illustration of synthesis route for Li_2S/graphene composite.

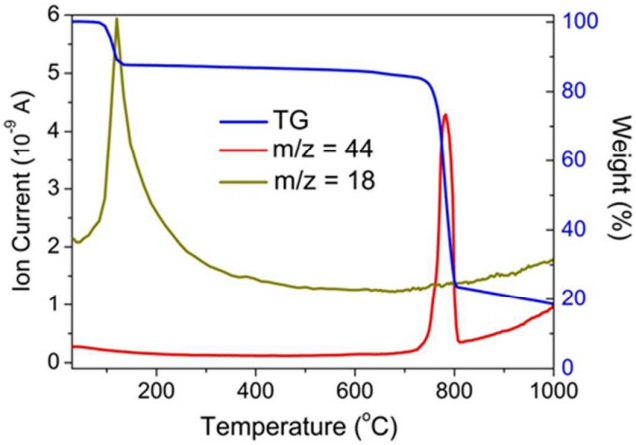

Figure 2. TG-MS profiles of LS-GNAs C (ramp rate: 10 °C/min).

weight loss steps were observed over the temperature range of 30–1000°C. The initial weight loss at around 84–134°C could originate from the removal of adsorbed water and mainly crystal water in $Li_2SO_4 \cdot H_2O$, as indicated by the significant signal of m/z 18 (H_2O^+), whereas the remarkable weight loss above 710°C could be assigned to the release of CO_2, as confirmed by the intense MS peak of m/z 44 (CO_2^+) at 781°C, originating from the chemical reaction $Li_2SO_4 + 2C \rightarrow 2CO_2 \uparrow + Li_2S$.[26] On the basis of the TG-MS results, LS-GNAs C was first heated at 200°C for 1 h to remove water and at 781°C for 2 h to complete the reaction between Li_2SO_4 and C. After cooling to room temperature (RT), the resulting solid product (**LS-**

GNAs H) was ground into a fine powder for further experiments and analysis. Note that according to the above chemical reaction equation, an excess amount of GNAs is required to ensure sufficient graphene residue as the host to support active Li_2S after pyrolysis. In our experiment, the $Li_2SO_4·H_2O$ and GNAs contents in LS-GNAs C were deliberately controlled as 1.60 and 0.48 g, respectively. After pyrolysis, LS-GNAs H was thoroughly washed in anhydrous methanol several times to remove Li_2S (the resulting solid is denoted as LS-GNAs H-W). The Li_2S content was estimated to be ~78.3 wt% by weight measurement of the residual graphene, which is very close to the expected theoretical value (~76.2 wt%).

The chemical composition and crystalline structure of the GNAs, LS-GNAs C, and LS-GNAs H were investigated by X-ray diffraction (XRD). As shown in **Figure 3**, the XRD patterns of the GNAs show an intense peak centered at 26.5°, which can be indexed as the (002) reflection and corresponds to stacking of graphene layers.[32, 33] This peak marked by the square is still remained in LS-GNAs C, and other sharp peaks agree very well with the diffractions for monoclinic $Li_2SO_4·H_2O$ (JCPDS 15-0873). However, the (002) peaks nearly disappeared for LS-GNAs H, whereas five intense peaks were observed at 27.0°, 31.2°, 44.8°, 53.1°, and 55.6°, corresponding to the (111), (200), (220), (311), and (222) reflections of Li_2S with cubic structure, respectively (JCPDS 23-0369). This result strongly confirms the successful transformation from Li_2SO_4 to Li_2S after pyrolysis. LS-GNAs H also contains trace amount of Li_2O, as indicated by a tiny diffraction peak at 33.6°, which can be assigned to the (111) reflection of cubic Li_2O (JCPDS 77-2144). This is probably resulted from the oxygen-containing functional groups (carboxyl, epoxy, or hydroxyl) on the surface of the GNAs. These polar groups, however, may act as growth sites and help to immobilize Li_2SO_4 during precipitation, leading to improved contact between C and Li_2S.

X-ray photoelectron spectroscopy (XPS) was employed to analyze the surface composition of LS-GNAs H. As expected, the S 2p spectra of LS-GNAs H are very similar to those of commercial Li_2S (**Figure 4a**); the only obvious difference is the

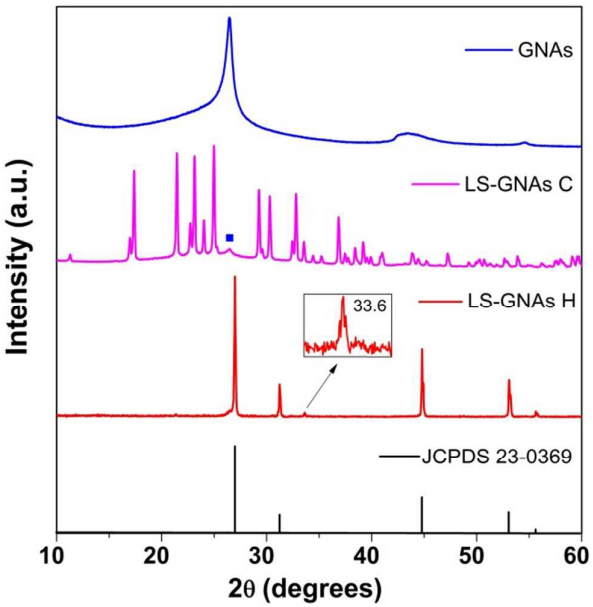

Figure 3. XRD patterns of GNAs, LS-GNAs C, and LS-GNAs H.

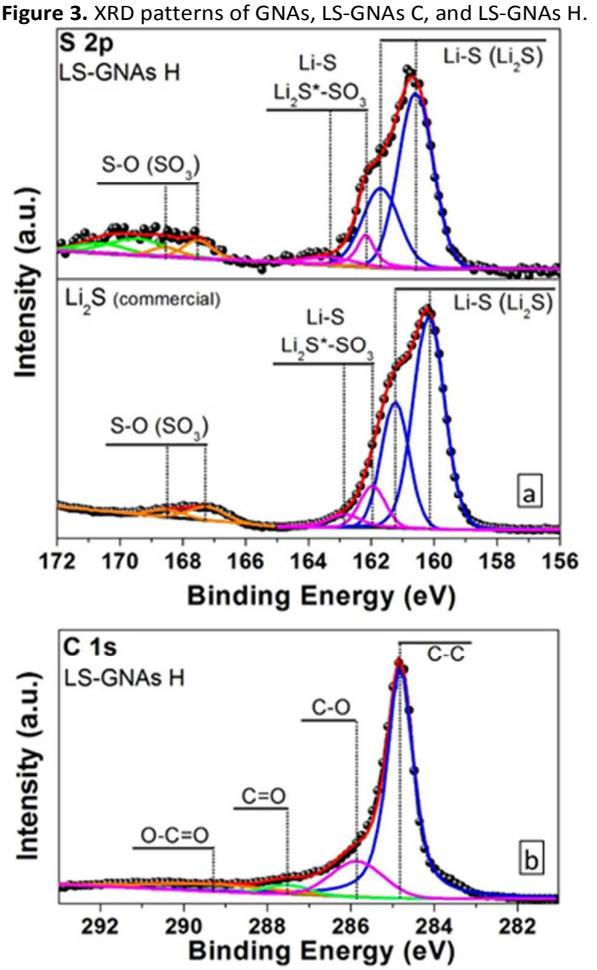

Figure 4. (a) High-resolution S 2p XPS spectra of LS-GNAs H and commercial Li_2S. (b) C 1s XPS spectra of LS-GNAs H.

additional signal above 169.0 eV for LS-GNAs H, which is probably due to the presence of a trace amount of unreacted Li_2SO_4. The S 2p spectra of LS-GNAs consist mainly of two signals at 160.6 and 161.7 eV, which can be ascribed to the S $2p_{3/2}$ and S $2p_{1/2}$ signals of Li–S bonding in Li_2S, respectively.[34] The other signals between 162.0 and 169.0 eV that are also observed in commercial Li_2S can be ascribed to Li_2S^*–SO_3 and SO_3.[34] It should be noted that nearly all of the S 2p signals of LS-GNAs H were shifted toward high energy compared with those of commercial Li_2S. As shown in **Figure 4b**, the deconvoluted C 1s spectrum clearly reveals the presence of C–O (285.9 eV), C=O (287.5 eV), and O–C=O (289.3 eV) species in LS-GNAs H in addition to the dominant C–C (284.8 eV) composition,[35, 36] which may account for the possible strong interaction between Li_2S and polar groups on the graphene matrix and thus the high-energy shift of the S 2p signals.

Figure 5 presents field emission scanning electron microscopy (FESEM) images of LS-GNAs H and LS-GNAs H-W. Clearly, the LS-GNAs H particles become quasi-spherical with an average size of 6.3 µm after pyrolysis, whereas the LS-GNAs C particles have irregular shapes and various particle sizes (**Figure S1**). In addition, high-magnification FESEM images reveal that wrinkled laminar structures appear in the surface morphology of LS-GNAs H (**Figure 5b** and **5c**). These lamellae are ascribed to the thin-layer graphene sheets resulting from in-situ etching of the GNAs during the chemical reaction at elevated temperature. The in-situ etching of the GNAs was further confirmed by the FESEM images of LS-GNAs H-W (after the Li_2S in LS-GNAs H was removed by washing), which is found to consist of much thinner sheets than the aggregated structure of the raw GNAs (**Figure S1**). Atomic force microscopy (AFM) images clarify that the GNAs were exfoliated from ca. 90 nm to < 1.3 nm after pyrolysis (**Figure S2**). Energy-dispersive X-ray spectroscopy (EDS) elemental mappings of LS-GNAs H show a uniform distribution of carbon and sulfur throughout the LS-GNAs H particles (**Figure 5d** and **5e**, respectively), implying that Li_2S is homogeneously deposited on the surface of the graphene sheets in situ. It is noteworthy that the in situ formed Li_2S/graphene composite, wherein Li_2S is immobilized by the 2D graphene host, provides high electronic conductivity because of the intimate contact between the graphene matrix and active material.

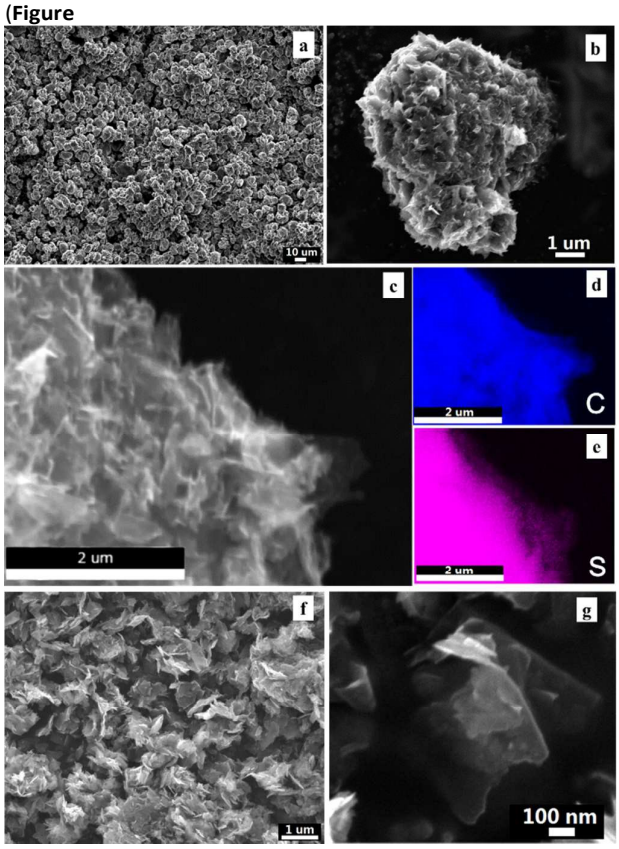

Figure 5. FESEM images of LS-GNAs H at (a) low and (b, c) high magnifications. EDS elemental mappings of (d) carbon and (e) sulfur over image (c). (f, g) FESEM images of LS-GNAs H-W.

The electrochemical performance of the obtained Li_2S/graphene composite (LS-GNAs H) was evaluated in 2032-type coin cells. Simultaneously, an electrode based on the Li_2S–GNAs mixture was also prepared under the same conditions for comparison. The electrolyte employed in this work is a stable glyme–Li salt molten complex ($[Li(G4)_1][TFSA]$) diluted by a hydrofluoroether (HFE) with low donor ability and viscosity developed by our group.[7, 8, 37-42] This solvate ionic-liquid-based mixture could be used directly as the electrolyte in Li–S batteries without additional lithium salt, greatly suppressing the dissolution of lithium polysulfides compared to conventional organic electrolytes and giving rise to high Coulombic efficiency.[7, 31] **Figure 6a** shows typical cyclic voltammograms of the LS-GNAs H–based electrode in $[Li(G4)_1][TFSA]$/4HFE for the first three cycles. For LS-GNAs H particles of micrometer size, the Li_2S electrode must first be electrochemically activated by applying a high charging cutoff voltage to overcome the barrier of lithium extraction from insulating Li_2S.[18, 43] Therefore, the potential was swept from the open circuit voltage (OCV) to 4.4 V (versus Li/Li^+) initially and then swept between 3.5 and 1.5 V, which is also the operating voltage range of the cells. In the first anodic scan, an intense oxidation peak at 4.30 V accompanied by a broad shoulder at 3.85 V are observed, corresponding to activation of the Li_2S electrode. In the cathodic scans, two sharp reduction peaks appear at approximately 2.27 and 1.97 V, which can be assigned to the transitions of sulfur to long-chain lithium polysulfide (Li_2S_x, $4 < x < 8$) and then to the end discharge product Li_2S, respectively.[28] A small oxidation peak at 2.41 V in the first cathodic scan is likely due to the oxidation of unactivated Li_2S or some intermediate lithium polysulfides generated during Li_2S activation. In contrast, only one oxidation peak located at 2.48 V exists during the subsequent anodic scans, which involve the direct conversion of Li_2S into elemental sulfur. The cyclic voltammetry (CV) profiles of the LS-GNAs H electrode agree well with those of the reported Li_2S cathodes.[43] Note that LS-GNAs H displays much more intense and sharper CV peaks than the Li_2S–GNAs mixture **(Figure 6b)**, revealing improved electronic conductivity and ion transport

due to the possible structural advantage of LS-GNAs H. In contrast, the Li_2S–GNAs mixture exhibits a higher activation potential (4.38 V) and oxidation potential (2.79 V) and lower reduction potentials (2.09 V and 1.67 V) than LS-GNAs H, indicating severe electrochemical polarization of the Li_2S–GNAs mixture, which is probably associated with the poor electrochemical contact between the insulating Li_2S and the GNAs.

The galvanostatic charge–discharge profiles of the LS-GNAs H–based electrode in the 1st, 5th, 10th, and 20th cycles at a current rate of 1/12 C are presented in **Figure 7a**. In the first charge process, the charge plateau (~4.19 V) is distinctly higher than that of the conventional sulfur cathode,[7] which can be attributed to the initial energy barrier from phase nucleation of polysulfides.[18] An initial charge capacity of 1116 mAh/g is achieved, which is close to the theoretical capacity of Li_2S (1166 mAh/g). It is noteworthy that the subsequent charge curves exhibit a very flat, stable plateau around 2.32 V, indicating direct oxidation of Li_2S to sulfur, whereas the discharge curves display two well-defined plateaus. The upper one, at 2.24 V, is related to the formation of long-chain lithium polysulfide, whereas the lower one, at 2.04 V, is related to the formation of lithium sulfide and lithium disulfide; the two peaks are in agreement

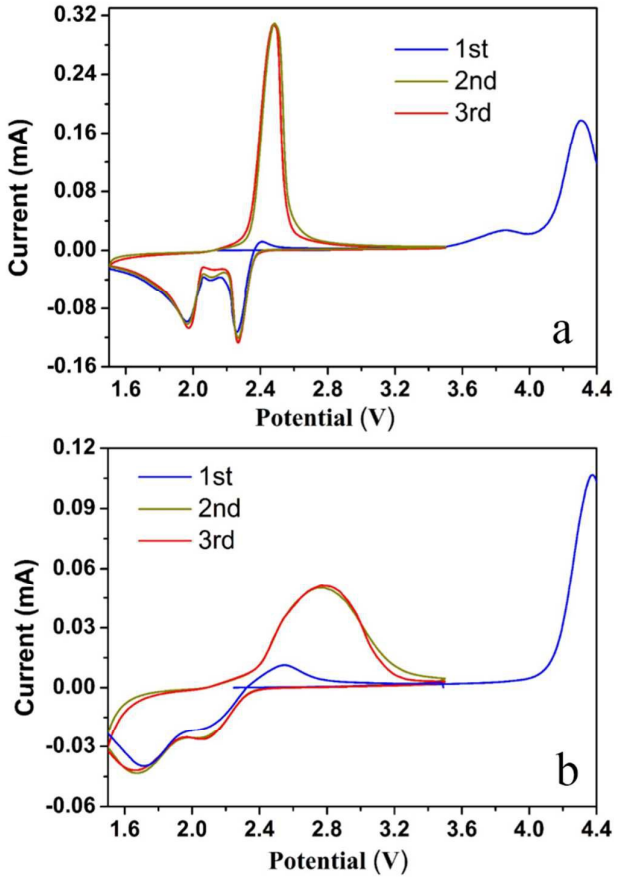

Figure 6. Typical cyclic voltammograms of (a) LS-GNAs H and (b) Li_2S–GNAs mixture in $[Li(G4)_1][TFSA]/4HFE$ at a scan rate of 0.04 mV/s. The potential was swept from the OCV to 4.4 V (versus Li/Li^+) initially and then swept between 3.5 and 1.5 V (versus Li/Li^+).

with the two reduction peaks in the CV curves **(Figure 6a)**. Significantly, the reduction and oxidation plateaus remain relatively constant over 20 cycles, suggesting a stable structure of LS-GNAs H and excellent cyclability of this electrode. To further reveal the structural stability of LS-GNA H, the cell after 40 cycles was disassembled, and the morphology of cathode was characterized by FESEM. As displayed in **Figure S3**, the overall structure of Li_2S/graphene composite-based electrode was well retained when compared with the fresh electrode, indicating the excellent structural stability of the composite. Compared with the Li_2S–GNAs mixture, LS-GNAs H shows not only a higher charge–discharge capacity but also less polarization. As seen in **Figure 7b**, the voltage hysteresis between the discharge and charge curves decreased from 0.62 to 0.28 V.

The cycling performance and Coulombic efficiency of LS-GNAs H at a current rate of 1/12 C are displayed in **Figure 8a**, together with the results for the Li_2S–GNAs mixture for comparison. LS-GNAs H exhibits a higher initial discharge capacity (693 mAh/g) than the Li_2S–GNAs mixture (245 mAh/g), indicating that the utilization of active material increased dramatically. After 40 cycles, the discharge capacity of LS-GNAs H declines to 508 mAh/g, whereas the Li_2S–GNAs mixture can deliver only 260 mAh/g. Although it was not as high initially, the Coulombic efficiency of LS-GNAs H is still maintained around 95% after 2 cycles, showing an improvement over the Li_2S–GNAs mixture–based electrode. Moreover, the irreversible capacity of 5% still remains, probably arising from the initial electrochemical activation process of Li_2S, which may cause some potential adverse effects on the electrolyte.

The rate capability of LS-GNAs H and the Li_2S–GNAs mixture at various discharge rates is investigated to further evaluate the kinetics of the electrodes; the data are presented in **Figure 8b**. For the LS-GNAs H cathode, the stepwise discharge capacities at discharge rates of 1/12 C, 1/6 C, 1/3 C, and 1 C are 684–589, 466–460, 292–287, and 197–195 mAh/g, respectively, which are markedly higher than those of the Li_2S–GNAs mixture (nearly zero at 1 C), demonstrating better rate performance. When the current rate was changed back to 1/12 C, a discharge capacity of 522 mAh/g was recovered for LS-GNAs H. This easy recovery of the discharge capacity after cycling under various conditions also implies that LS-GNAs H has good stability and reversibility.

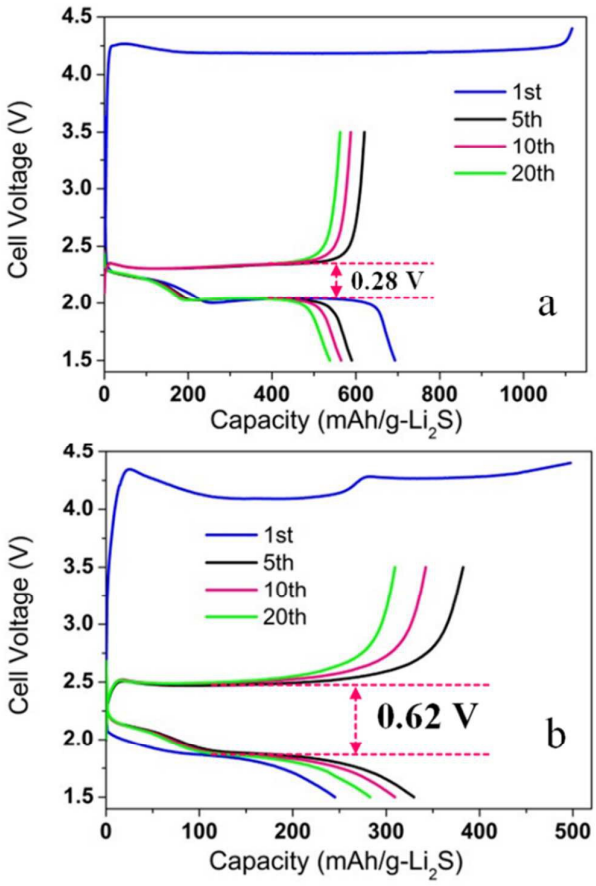

Figure 7. Galvanostatic charge–discharge profiles of (a) LS-GNAs H and (b) Li_2S–GNAs mixture in the 1st, 5th, 10th, and 20th cycles at a current rate of 1/12 C (1 C = 1166 mA/g).

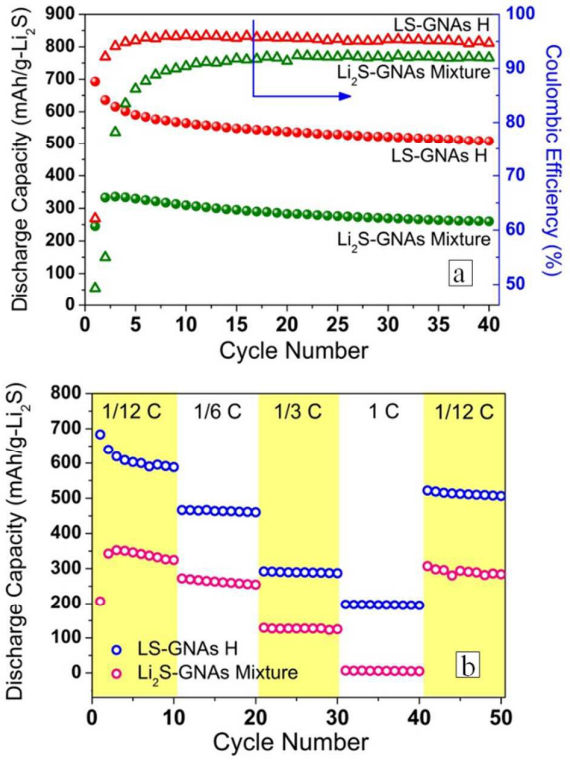

Figure 8. (a) Cycling performance and Coulombic efficiency of LS-GNAs H and Li_2S–GNAs mixture over 40 cycles at a current rate of 1/12 C. (b) Rate capability of LS-GNAs H and Li_2S–GNAs mixture at various discharge rates from 1/12 C to 1 C. The charge rate is fixed at 1/12 C (1 C = 1166 mA/g).

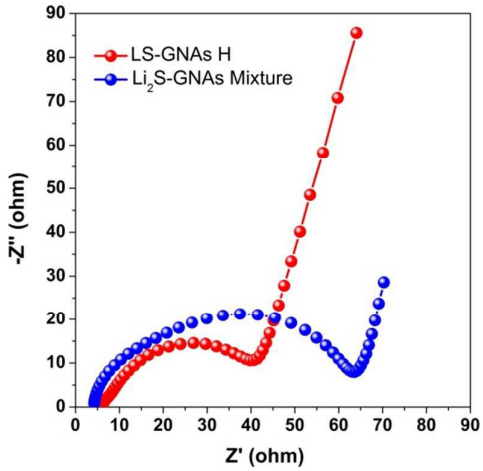

Figure 9. Nyquist plots of LS-GNAs H and Li_2S–GNAs mixture before the initial charge.

To investigate the influence of the Li_2S content in LS-GNA H on electrochemical performance, different composites were prepared by adjusting the amount of GNAs deliberately. During the fabrication of the electrode, carbon black was added to keep the same final composition of Li_2S, carbon and PVP in the electrode (Li_2S: C: PVP = 60:30:10), wherein the

carbon included the graphene and carbon black. Compositions of different Li_2S/graphene composite-based electrodes are exhibited in **Table S1**. It is readily apparent that the Li_2S content can affect the electrochemical performance, as indicated in **Figure S4**. Base on the comparison of cycling performance and Coulombic efficiency among different composites (**Figure S5**), the Li_2S content of 78.3 wt% is the best composite composition for the electrochemical performance.

The fast reaction kinetics, low polarization, and greatly enhanced capacity and rate capability of LS-GNAs H compared with the Li_2S–GNAs mixture could be ascribed to the unique Li_2S/graphene structure. The Li_2S formed in situ by chemical reaction between Li_2SO_4 and the GNAs at high temperature is probably deposited uniformly on the graphene sheets. The high conductivity of graphene as well as the intimate contact between the insulating electroactive material (Li_2S) and cathodic host is expected to improve the utilization of active material and contribute to the transport of electrons to the active material during the charge–discharge process. Electrochemical impedance spectroscopy (EIS) profiles of LS-GNAs H and the Li_2S–GNAs mixture confirmed this point (**Figure 9**). Although they have nearly comparable bulk resistances corresponding to the electrolyte resistance (as determined by the left intersection of the semicircle with the *x* axis), the LS-GNAs H cathode exhibits a much lower charge transfer resistance (R_{ct}) for the electrochemical reaction on the electrode–electrolyte intersurface (as determined by the diameter of the semicircle).[44, 45] For Li_2S–GNAs mixture, the Nyquist plot seems to contain two semicircles, probably due to the different electrochemical environments in Li_2S–GNAs mixture, which are affected by the distribution of the conducting agent and large-sized Li_2S. The 2D graphene is also necessary for high cell performance, because when the GNAs were replaced by a benchmark Ketjenblack (KB, specific surface area: 1270 m^2/g), the obtained KB–Li_2S composite (**LS-KB H**) exhibits a much lower discharge capacity than LS-GNAs H (**Figure S6**).

Conclusions

In summary, we reported a very simple method of preparing a Li_2S/graphene composite through one-pot pyrolysis of lithium sulfate and GNAs without using expensive commercial Li_2S. This step can immobilize the active Li_2S deposits in situ on the highly conductive host by intimate contact. XRD results showed that no impurities were formed except for a tiny amount of Li_2O. FESEM and EDS confirmed the homogenous distribution of C and S in the obtained composite. The in situ formed Li_2S/graphene could be used directly as cathodes for lithium–sulfur batteries, delivering greatly enhanced capacities, fast reaction kinetics, low polarization, and good cycling performance and rate capability as compared with a physical mixture of commercial Li_2S and GNAs. For example, LS-GNAs H–based half-cells showed an initial discharge capacity of 693 mAh/g, a 40th discharge capacity of 508 mAh/g, and a Coulombic efficiency of ca. 95%, which are much higher than those of a mixture of commercial Li_2S and GNAs. EIS analysis suggested that this improvement could be related to the reduced charge transfer resistance. Note, in addition, that the 2D layer structure of graphene plays an important role in transporting electrons and ions and thus maximizing the utilization of the active Li_2S, as suggested by a control experiment using a Li_2S/KB composite. The performance (e.g., areal capacity) of the battery based on this in-situ strategy might be further improved by reducing the particle size of the Li_2S/graphene composite,[24] introducing redox mediators to the electrolyte[46] to depress the active potential of Li_2S, or optimizing the type of binder and current collector.

Experimental Section

Preparation of Li_2S/graphene composite: A Li_2SO_4/graphene nanoplatelet aggregates (GNAs) composite was first obtained via a solvent/nonsolvent precipitation method. GNAs (Strem Chemicals, 0.48 g) and $Li_2SO_4{\cdot}H_2O$ (1.60 g) were dispersed into ultrapure water (70 mL) by ultrasonication for 2 h to form a suspension. After stirring for 4 h, ethanol (800 mL) was added dropwise to the suspension. Subsequently, the black precipitates were filtered off, washed with ethanol several times, and then dried in vacuum at 40°C for 12 h. This collected composite was labeled LS-GNAs C. The LS-GNAs C was then heated in a tube furnace under an argon atmosphere according to the following temperature program: (1) keeping at room temperature (RT) for 1 h to degas, (2) heating at 10°C/min to 200°C, (3) holding at 200°C for 1 h, (4) heating at 10°C/min to 781°C, and (5) calcining at 781°C for 2 h. After cooling to RT naturally, the solid product, denoted as LS-GNAs H, was obtained. Because Li_2S is soluble in anhydrous methanol, LS-GNAs H was thoroughly washed by methanol several times to remove Li_2S. The remaining carbon, denoted as LS-GNAs H-W, was finally dried at 30°C for 6 h. Ultimately, the Li_2S content in LS-GNAs H was estimated to be 78.3 wt% by weight measurement before and after washing.

Material characterization: Thermogravimetry-mass spectrometry measurement was conducted using a Bruker TG-DTA2020SA/MS9610 instrument. The morphology was characterized by a field emission scanning electron microscope (JEOL JSM-7001F) equipped with an energy-dispersive X-ray spectroscopy system. The X-ray diffraction patterns were recorded on a Rigaku Ultima Ⅳ X-ray diffractometer using a Cu Kα radiation source. Atomic force microscopy (AFM, SII SPI3800N/SPA400) was conducted to measure the thickness of the graphene materials. For the AFM measurements, the samples were dispersed in water by ultrasonication for 30 min and then placed on freshly cleaved mica surfaces before observation. The composition was investigated using an X-ray photoelectron spectroscope (ULVAC-PHI Quantera SXM).

Electrochemical measurements: Because lithium sulfide is very sensitive to moisture, all the cell preparation procedures were conducted in an argon-filled glovebox in which the moisture level was below 1 ppm. The LS-GNAs H–based electrode was prepared by grinding LS-GNAs H with carbon

black (Super C65, TIMCAL) and polyvinylpyrrolidone (PVP, MW = 1200 kDa, JUNSEI) in a weight ratio of 76.6:13.4:10 (Li_2S:C:PVP = 60:30:10) for 50 min using *N*-methyl-2-pyrrolidinone as the solvent. The obtained slurry was uniformly deposited on an aluminum foil current collector by a doctor-blade technique and then dried in vacuum at 80°C for 16 h. The mass loading of active material was around 0.5 mg/cm^2. Under the same conditions, a Li_2S–GNAs mixture–based electrode was also prepared for comparison by mixing commercial Li_2S, GNAs, carbon black (Super C65), and PVP in a weight ratio of 60:16.6:13.4:10. For the electrolyte, tetraglyme (G4, Nippon Nyukazai) and lithium bis(trifluoromethanesulfonyl)amide (Li[TFSA], Solvey) were mixed in a molar ratio of 1:1. After the mixture was stirred at RT for 24 h, a homogeneous liquid denoted as $[Li(G4)_1][TFSA]$ was obtained. Next, 1,1,2,2-tetrafluoroethyl 2,2,3,3-tetrafluoropropyl ether (HFE) was added to the $[Li(G4)_1][TFSA]$ to obtain a $[Li(G4)_1][TFSA]$/HFE electrolyte, where the molar ratio of $[Li(G4)_1][TFSA]$:HFE is 1:4. Then, 2032-type coin cells (half-cells) were assembled using the Li_2S cathode, a porous glass separator (GA55, Advantec), a lithium foil counter electrode, and the $[Li(G4)_1][TFSA]$/4HFE electrolyte. The coin cells were equilibrated at RT for 12 h before the electrochemical measurements. The galvanostatic charge and discharge tests of the coin cells were conducted using a Nagano BTS-2004 battery testing system at 30°C. The cells were initially charged from the open circuit voltage to 4.40 V (vs. Li/Li$^+$) to activate the Li_2S and then cycled in the voltage range of 1.50–3.50 V (vs. Li/Li$^+$). The specific capacity of the cell was calculated on the basis of the mass of Li_2S, and 1166 mA/g was defined as 1 C rate. Cyclic voltammetry measurement was performed using a Bio-Logic SAS VMP3 electrochemical workstation at a scan rate of 0.04 mV/s. Electrochemical impedance spectroscopy measurements were made for the fresh cells before cycling, using the same electrochemical workstation at the open circuit voltage (OCV) in the frequency range of 100 kHz to 4 Hz with a sinusoidal excitation amplitude of 5 mV.

Acknowledgements

This research was supported in part by the Advanced Low Carbon Technology Research and Development Program (ALCA) of the Japan Science and Technology Agency (JST). Z.L. acknowledges financial support from the China Scholarship Council (CSC).

References

1. P. G. Bruce, S. A. Freunberger, L. J. Hardwick and J. M. Tarascon, *Nat. Mater.*, 2012, **11**, 19.
2. A. Manthiram, Y. Fu and Y. S. Su, *Acc. Chem. Res.*, 2013, **46**, 1125.
3. M. Barghamadi, A. Kapoor and C. Wen, *J. Electrochem. Soc.*, 2013, **160**, A1256.
4. A. Manthiram, Y. Fu, S. H. Chung, C. Zu and Y. S. Su, *Chem. Rev.*, 2014, **114**, 11751.
5. X. Ji, K. T. Lee and L. F. Nazar, *Nat. Mater.*, 2009, **8**, 500.
6. M. K. Song, E. J. Cairns and Y. Zhang, *Nanoscale*, 2013, **5**, 2186.
7. K. Dokko, N. Tachikawa, K. Yamauchi, M. Tsuchiya, A. Yamazaki, E. Takashima, J. W. Park, K. Ueno, S. Seki, N. Serizawa and M. Watanabe, *J. Electrochem. Soc.*, 2013, **160**, A1304.
8. N. Tachikawa, K. Yamauchi, E. Takashima, J. W. Park, K. Dokko and M. Watanabe, *Chem. Commun.*, 2011, **47**, 8157.
9. J. W. Park, K. Yamauchi, E. Takashima, N. Tachikawa, K. Ueno, K. Dokko and M. Watanabe, *J. Phys. Chem. C*, 2013, **117**, 4431.
10. J. W. Park, K. Ueno, N. Tachikawa, K. Dokko and M. Watanabe, *J. Phys. Chem. C*, 2013, **117**, 20531.
11. C. Zhang, A. Yamazaki, J. Murai, J. W. Park, T. Mandai, K. Ueno, K. Dokko and M. Watanabe, *J. Phys. Chem. C*, 2014, **118**, 17362.
12. J. Kim, D. J. Lee, H. G. Jung, Y. K. Sun, J. Hassoun and B. Scrosati, *Adv. Funct. Mater.*, 2013, **23**, 1076.
13. G. Xu, B. Ding, J. Pan, P. Nie, L. Shen and X. Zhang, *J. Mater. Chem. A*, 2014, **2**, 12662.
14. S. S. Zhang, *J. Power Sources*, 2013, **231**, 153.
15. K. Zhang, L. Wang, Z. Hu, F. Cheng and J. Chen, *Sci. Rep.*, 2014, **4**, 6467.
16. Y. Yang, M. T. McDowell, A. Jackson, J. J. Cha, S. S. Hong and Y. Cui, *Nano Lett.*, 2010, **10**, 1486.
17. M. Nagao, A. Hayashi and M. Tatsumisago, *J. Mater. Chem.*, 2012, **22**, 10015.
18. Y. Yang, G. Zheng, S. Misra, J. Nelson, M. F. Toney and Y. Cui, *J. Am. Chem. Soc.*, 2012, **134**, 15387.
19. K. Cai, M. K. Song, E. J. Cairns and Y. Zhang, *Nano Lett.*, 2012, **12**, 6474.
20. J. Liu, H. Nara, T. Yokoshima, T. Momma and T. Osaka, *J. Power Sources*, 2015, **273**, 1136.
21. F. Wu, J. T. Lee, A. Magasinski, H. Kim and G. Yushin, *Part. Part. Syst. Charact.*, 2014, **31**, 639.
22. F. Wu, A. Magasinski and G. Yushin, *J. Mater. Chem. A*, 2014, **2**, 6064.
23. J. Guo, Z. Yang, Y. Yu, H. D. Abruna and L. A. Archer, *J. Am. Chem. Soc.*, 2013, **135**, 763.
24. C. Nan, Z. Lin, H. Liao, M. K. Song, Y. Li and E. J. Cairns, *J. Am. Chem. Soc.*, 2014, **136**, 4659.
25. Z. Lin, C. Nan, Y. Ye, J. Guo, J. Zhu and E. J. Cairns, *Nano Energy*, 2014, **9**, 408.
26. Z. Yang, J. Guo, S. K. Das, Y. Yu, Z. Zhou, H. D. Abruña and L. A. Archer, *J. Mater. Chem. A*, 2013, **1**, 1433.
27. S. Evers and L. F. Nazar, *Chem. Commun.*, 2012, **48**, 1233.
28. X. Yang, L. Zhang, F. Zhang, Y. Huang and Y. Chen, *ACS Nano*, 2014, **8**, 5208.
29. H. Wang, Y. Yang, Y. Liang, J. T. Robinson, Y. Li, A. Jackson, Y. Cui and H. Dai, *Nano Lett.*, 2011, **11**, 2644.
30. K. Han, J. Shen, C. M. Hayner, H. Ye, M. C. Kung and H. H. Kung, *J. Power Sources*, 2014, **251**, 331.
31. S. Zhang, K. Ueno, K. Dokko and M. Watanabe, *Adv. Energy Mater.*, 2015, DOI: aenm.201500117.
32. G. Wang, J. Yang, J. Park, X. Gou, B. Wang, H. Liu and J. Yao, *J. Phys. Chem. C*, 2008, **112**, 8192.
33. A. V. Murugan, T. Muraliganth and A. Manthiram, *Chem. Mater.*, 2009, **21**, 5004.
34. Y. Diao, K. Xie, S. Xiong and X. Hong, *J. Electrochem. Soc.*, 2012, **159**, A1816.
35. H. Huang, Y. Xia, X. Tao, J. Du, J. Fang, Y. Gan and W. Zhang, *J. Mater. Chem.*, 2012, **22**, 10452.

36. C. Mattevi, G. Eda, S. Agnoli, S. Miller, K. A. Mkhoyan, O. Celik, D. Mastrogiovanni, G. Granozzi, E. Garfunkel and M. Chhowalla, *Adv. Funct. Mater.*, 2009, **19**, 2577.
37. T. Tamura, K. Yoshida, T. Hachida, M. Tsuchiya, M. Nakamura, Y. Kazue, N. Tachikawa, K. Dokko and M. Watanabe, *Chem. Lett.* , 2010, **39**, 753.
38. K. Ueno, K. Yoshida, M. Tsuchiya, N. Tachikawa, K. Dokko and M. Watanabe, *J. Phys. Chem. B*, 2012, **116**, 11323.
39. K. Yoshida, M. Tsuchiya, N. Tachikawa, K. Dokko and M. Watanabe, *J. Phys. Chem. C*, 2011, **115**, 18384.
40. K. Yoshida, M. Nakamura, Y. Kazue, N. Tachikawa, S. Tsuzuki, S. Seki, K. Dokko and M. Watanabe, *J. Am. Chem. Soc.*, 2011, **133**, 13121.
41. K. Yoshida, M. Tsuchiya, N. Tachikawa, K. Dokko and M. Watanabe, *J. Electrochem. Soc.*, 2012, **159**, A1005.
42. K. Ueno, J. W. Park, A. Yamazaki, T. Mandai, N. Tachikawa, K. Dokko and M. Watanabe, *J. Phys. Chem. C*, 2013, **117**, 20509.
43. Y. Fu, Y. S. Su and A. Manthiram, *Adv. Energy Mater.*, 2014, **4**, 1300655.
44. Y. S. Su and A. Manthiram, *Electrochim. Acta* 2012, **77**, 272.
45. L. Chen, Y. Liu, M. Ashuri, C. Liu and L. L. Shaw, *J. Mater. Chem. A*, 2014, **2**, 18026.
46. S. Meini, R. Elazari, A. Rosenman, A. Garsuch and D. Aurbach, *J. Phys. Chem. Lett.*, 2014, **5**, 915.